Check for updates

Tuning electrocatalytic water oxidation by MnOx through the incorporation of abundant metal cations†

Jens Melder, [ID] ‡*[a] Stefan Mebs,*[b] Florian Lessing, [ID] [a] Holger Dau [ID] [b] and Philipp Kurz [ID] [a]

Layered manganese oxides which were deposited on carbon fibre paper (MnOx/CFP) *via* a redox-deposition process show promising activities and stabilities for the OER over a very wide pH range. In the study presented here, the influence of the incorporation of metal cations (M^{n+}, M = Ca, Co, Ni, Fe) into MnOx layers on the OER performance at different pH values (2.5/7.0/14.0) is explored. Spectroscopic analyses of M_yMnOx/CFP reveal that doping with other metal cations does not alter the basic birnessite-type MnOx structure. However, the average manganese oxidation state can be tuned and is found to depend on the incorporated metal cations. Furthermore, a clear dependence of the catalytic activity and stability on the incorporated metal ion is observed and especially Ni- and Co-doping lead to a significant performance boost under alkaline (Ni and Co) and neutral conditions (Co). A comparison to other state-of-the-art metal oxide catalysts (also deposited on CFP for comparison) shows that the metal-doped M_yMnOx/CFP anodes are able to compete with the most active materials known so far.

1 Introduction

The need for a sustainable energy supply that is not based on fossil fuels like crude oil or natural gas is urgent not only because their resources are finite but also because their combustion produces CO_2. The conversion of solar energy, the most ubiquitous energy source, into storable fuels like H_2 by catalytic processes has recently attracted much attention. For this, the splitting of water to H_2 and O_2 might play a central technological role.[1–3]

The energy ($\Delta G = 237$ kJ mol$(H_2)^{-1}$)[4] required to power this highly endothermic reaction can be provided by several renewable sources, one of which is electricity from wind or solar energy (*e.g.* by photovoltaics or wind turbines). The electrochemical splitting of water can be divided into two half-cell reactions, the hydrogen evolving reaction (HER) and the oxygen evolving reaction (OER).

From these two reactions, the OER is kinetically more demanding due to the combined release of four electrons and four protons from two water molecules during the production of a single oxygen molecule. In an ideal system, O_2 and H_2 can be evolved when the potential difference between the cathode and the anode exceeds 1.23 V *vs.* the reversible hydrogen electrode (RHE).[5] However, often high overpotentials η need to be applied to achieve reasonable current densities j. Earth-abundant, cheap, scalable, non-toxic, stable and first and foremost efficient catalysts are urgently needed in order to make the production of hydrogen from water splitting energetically more efficient and at the same time industrially feasible.

Great efforts have been made over the last few years in finding such earth abundant catalysts for the OER. The most promising candidates are based on Co,[6] Ni,[7,8] Fe[9,10] or Mn,[11–15] which are able to reach benchmark current densities of $j = 10$ mA cm^{-2} at overpotentials as low as $\eta < 300$ mV in alkaline or $\eta \sim 550$ mV in neutral media.[15–21] Unfortunately, most of the before mentioned catalysts suffer from corrosion when used under more acidic pH conditions[22–25] and thus, acid-stable, well-performing catalysts from non-critical sources are still scarce. Currently, the only convincing materials for OER catalysis at pH < 7 are based on Ir and Ru, two of the rarest metals on earth, with a global Ir production of less than 9 tons per year.[26,27]

On the other hand, OER catalysis in the acidic pH regime is of great interest due to its possible application in proton exchange membrane (PEM) electrolyzers, photoelectrochemical (PEC) cells or other electrochemical devices, which have to be operated at pH < 7 (*e.g.* some microbial electrosynthesis cells).[28–31] PEM electrolyzers can be operated at high current densities, are able to respond quickly to the power input due to

[a]*Institut für Anorganische und Analytische Chemie and Freiburger Materialforschungszentrum (FMF), Albert-Ludwigs-Universität Freiburg, Albertstraße 21, 79104 Freiburg, Germany. E-mail: jens.melder@dlr.de*

[b]*Fachbereich Physik, Freie Universität Berlin, Arnimallee 14, 14195 Berlin, Germany. E-mail: stebs@chemie.fu-berlin.de*

† Electronic supplementary information (ESI) available. See DOI: https://doi.org/10.1039/d2se01401g

‡ Present address: German Aerospace Center, Institute of Combustion Technology, Pfaffenwaldring 38-40, 70569 Stuttgart, Germany.

the fast proton conduction across the membrane and show a compact cell design.[4] Hence, they are especially applicable for highly dynamic operations, one of the main requirements if power from renewable sources is to be used. Furthermore, PEM electrolyzers are widely seen as the most promising water electrolysis systems.[32,33]

Manganese oxides (MnO_x) have extensively been investigated as OER catalysts. With the oxygen evolving complex (OEC), the $Mn_4CaO_5(H_2O)_x$ cluster of photosystem II, biology provides a template for a catalyst able to efficiently accelerate the OER under near-neutral conditions.[34–36] Inspired by this, the water oxidation catalysis (WOC) activities of many MnO_x polymorphs have been investigated. In comparative studies, amorphous layered or tunneled phases often showed the best performance[13–15,37–44] with birnessites and phyllomanganates consisting of edge-sharing $[MnO_6]$ octahedra with layer-to-layer distances of ~ 7 Å, as prominent examples. The average oxidation states of the manganese ions in these oxides are very flexible ranging typically from +3.3 to +3.9.[38,45]

We recently developed a method to deposit birnessite-type MnO_x on high surface area graphitic carbon fiber papers by an easily scalable *in situ* redox deposition approach and obtained promising WOC electrodes.[13] In this process, the carbon itself acts as a reducing agent to permanganate ions and (unlike many other electrode preparation routes) no further binders (*e.g.* polyethylene oxide, PEO) or additional polymers (*e.g.* Nafion®) are needed to attach MnO_x to the support material. In a consecutive study, we showed that MnO_x/CFP is a nanostructured volume catalyst exhibiting good WOC activities and stabilities over nearly the entire pH range from 1–14.[14] For all pH values of this range, current densities > 1 mA cm^{-2} could be achieved at overpotentials η of 350–500 mV, which are very good values for electrodes containing only earth-abundant elements (Mn, O, K and C). Especially the very substantial performance of MnO_x/CFP in the mildly acidic pH regime (pH 2–6) has to be highlighted.[14] The good stability of manganese oxide catalysts under acidic pH conditions was also found by other groups. For example, Li *et al.* showed that γ-MnO_2 is stable for over 8000 h at 10 mA cm^{-2} and pH 2.[46]

Birnessites can be modified by incorporating a wide range of different cations into their layered structure. The physical and chemical properties of layered MnO_x are greatly influenced by the type, amount and location of the dopants.[47–51] This has been used for the selective removal of toxic metals from wastewater, the optimization of MnO_x-based capacitors, and also for MnO_x catalysis *e.g.* amine–imine transformations,[51] alcohol oxidation,[52] alkene oxidation,[53] and water oxidation.[48–50,54–57] Co doped MnO_x are particularly noteworthy in the latter case. It has already been shown that the incorporation of Co into the MnO_x framework can have a positive effect on its OER activity.[55–57] Moreover, Nakamura and co-workers demonstrated that the OER stability under acidic pH of cobalt spinel oxide can be significantly enhanced by the selective incorporation of manganese.[58] However, no study comparing the effect on the electrocatalytic activity and stability in a wide pH range of the incorporation of different OER active transition metal cations into birnessite electrocatalysts has been reported.

Here, we present the results of an extensive investigation of the influence of the incorporation of abundant metal ions (Ni, Fe, Co and Ca) into MnO_x/CFP electrodes by means of ion exchange. The choice fell on these metals, either because their oxides are themselves among the most active OER catalysts (in the cases of Ni, Fe and Co) or because they are part of the biological OEC (Ca). The prime motivation was to find out whether the already good performance of MnO_x/CFP can be further enhanced by metal doping. Therefore, the electrochemical activities and stabilities of ion-exchanged M_yMnO_x/CFP electrodes were tested at three different pH values either in potassium phosphate buffer (pH 2.5/7.0) or in a potassium hydroxide electrolyte (pH 14.0). The influence of the incorporation of these foreign ions on the oxide's structure, composition and morphology both before and after electrocatalysis was also probed by means of infra-red spectroscopy (IR), powder X-ray diffraction (XRD), scanning electron microscopy (SEM) and X-ray absorption spectroscopy (XAS). The elemental composition was determined by flame atomic absorption spectroscopy (fAAS) and energy dispersive X-ray (EDX) spectroscopy. Finally, the activities of the M_yMnO_x/CFP anodes were compared to those of common state-of-the-art OER electrocatalysts.

2 Results and discussion

2.1 Electrode preparation, ion-exchange properties and characterization

MnO_x/CFP electrodes were prepared by the direct redox reaction of potassium permanganate solutions with carbon fiber papers.[13] This process leads to carbon fibers uniformly covered by a birnessite-type MnO_x coating with an average Mn oxidation state of +3.7.[14] The manganese oxide coating additionally contains potassium ions with an atomic K : Mn ratio of 0.1 : 1.0 as well as water. Starting from the $K_{0.1}MnO_x$/CFP electrodes, the metal doped electrodes were obtained by an ion-exchange reaction from solutions of $M^{2+/3+}(NO_3)_{2/3}$ (M = Ni^{2+}, Fe^{3+}, Co^{2+}, Ca^{2+}) (Fig. 1). Electrodes with different molar $M^{2+/3+}$: Mn ratios were synthesized by varying the time for which the electrodes were exposed to the metal nitrate solutions. After the ion-exchange reactions, the electrodes were thoroughly washed with water and afterwards sintered at 400 °C for 1 h in air, which was known from former studies to be essential for activation.[14] To determine the elemental composition of the electrodes, the oxide layers were dissolved in acid and the resulting solutions were analyzed by fAAS (see Fig. S1 in the ESI†).

The ion-exchange reactions with Ni^{2+}/Fe^{3+}/Ca^{2+} were found to be slow reaching a steady state only after ~ 8 h. A good correlation between the decrease of K^+ ions and the increase of Ni^{2+}/Fe^{3+}/Ca^{2+} as a function of time can be observed. Nevertheless, even after 24 h only maximum molar ratios of $M^{2+/3+}$: Mn $\sim$ 0.1 : 1 were found suggesting that other species, most likely H^+, must also be involved in the ion-exchange reaction to keep the overall charge neutral. A dissolution of Mn ions during the ion-exchange process can be excluded as no loss of Mn from the electrodes was found by fAAS.

For Co, the ion-exchange reaction is much faster and could therefore be carried out using a 0.1 M Co^{2+} nitrate solution.
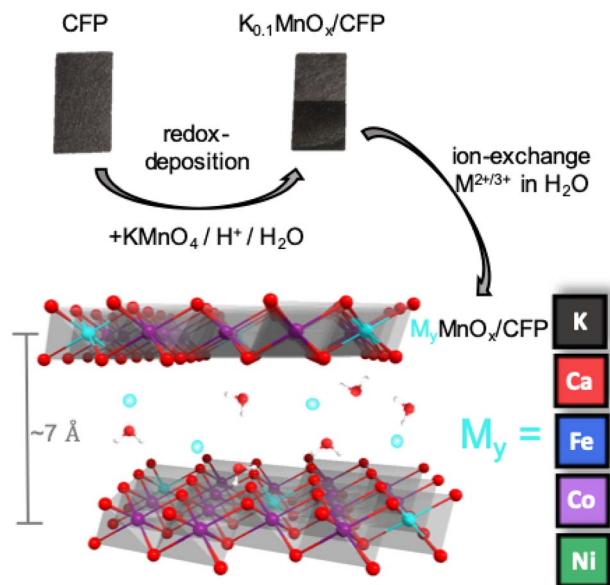
Fig. 1 Schematic representation of the preparation of M_yMnO_x/CFP by ion exchange from $K_{0.1}MnO_x$/CFP.

Furthermore, many more Co ions can be incorporated into the as-prepared $K_{0.1}MnO_x$/CFP electrode leading to maximum molar ratios of $Co : Mn \sim 0.3 : 1$ already after 4 h. A faster and higher uptake of Co-ions in comparison to Ni- and Fe-ions by birnessites was several times observed before.[59–61] The ion-exchange reactions were confirmed by EDX analysis (Fig. S2 in the ESI†), which showed similar M : Mn ratios.

In order to determine morphological and structural changes induced by the incorporation of the metal ions during the ion exchange and the subsequent annealing steps, a number of analytical measurements were carried out.

First, possible changes of the morphology were analyzed by SEM (see Fig. 2 and S3†). The exposure of the as-prepared electrodes to the metal nitrate solution has no impact on the stability and the uniformity of the coverage of the carbon fibers by MnO_x. No cracks or loss of metal oxide could be observed and all metal oxide layers show very similar, sponge-like structures typical of birnessites.[11,13,14,37] Minor differences are visible for the $Ca_{0.1}MnO_x$/CFP electrode where the porosity of the overall structure appears less pronounced.

Interestingly, larger morphological deviations can be found for the $Co_{0.3}MnO_x$/CFP electrode. Here, the disordered structure is still present but the threads from which the basic structure is built are wider and more structured on the surface. Despite the different morphology, CoO_x or MnO_x phase separations can be excluded as EDX mapping shows a uniform distribution of both metals within the structure (see Fig. S4†).

The findings from SEM/EDX could be supported by powder XRD measurements, where no additional reflexes are visible in all M_yMnO_x/CFP patterns in comparison to $K_{0.1}MnO_x$/CFP (see Fig. 2B), indicating that no additional crystalline phases/islands, *e.g.* Co/Ni/Ca/Fe (oxy)hydroxides or oxides, are formed.

The intense reflections visible at $2\theta \sim 26°$ and $\sim54°$ in all XRD patterns stem from the graphitic carbon support and can be attributed to the (002) and (004) planes of graphite.[62] Much less intense, very broad reflections at $2\theta \sim 12°$ (001) and $\sim37°$ (100) are characteristic of highly disordered birnessite. The reflection at $\sim12°$ which is indicative for an ordered stacking of the octahedral sheets is only well pronounced for the $K_{0.1}MnO_x$/CFP electrode. Its disappearance is indicative of a further amorphization introduced by the ion-exchange process by

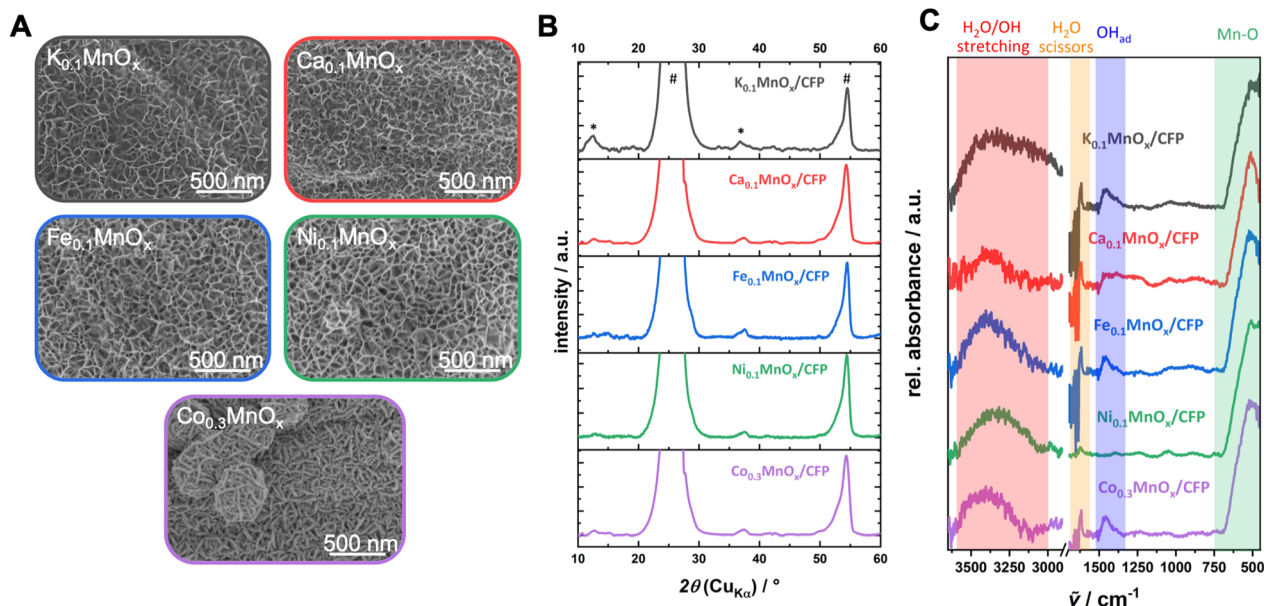**Fig. 2** (A) Scanning electron microscopy images, (B) powder XRD patterns (reflexes of the graphitic carbon support and the birnessite-like catalyst are labeled with * and #, respectively) and (C) ATR-FTIR spectra of a $K_{0.1}MnO_x$/CFP electrode and electrodes after the ion-exchange reaction before operation as anodes for water oxidation catalysis. Additional SEM images can be found in Fig. S3 in the ESI.†

increasing the stacking disorder of the $[MnO_6]$-octahedral sheets, most likely due to the incorporation of additional ions into the interlayer space. Such a loss of crystallinity has already been previously observed for Ca-, Ni- and Co-doped birnessites.[63–65] The reflection at ∼37° which arises from regular distances within the layers of edge-sharing $[MnO_6]$ octahedra remains visible for all electrodes. Compared to the reflex for the parent $K_{0.1}MnO_x$/CFP electrode, which can be found at $2\theta = 36.8°$, a slight shift to higher values can be observed for the ion-exchanged electrodes (between $2\theta = 37.4°$ and 37.7°). This is an indication that the incorporated ions also intercalate into the layers of the birnessite backbone.

The ATR-FTIR spectra of all electrodes are also typical of birnessites and after doping does not show new bands (Fig. 2). The observed signals at 750–500 cm^{-1} are indicative of Mn–O vibrations from the $[MnO_6]$ octahedra,[13,37,66] while the absorptions between 3600 and 3000 cm^{-1} and 1700–1600 cm^{-1} belong to incorporated water molecules.[67] For all M_yMnO_x/CFP electrodes (except for $Ca_{0.1}MnO_x$/CFP and $Ni_{0.1}MnO_x$/CFP electrodes), an absorption at ∼1460 cm^{-1} is visible, which can be attributed to the vibrations of adsorbed hydroxides.[67]

Thus, the analytical methods used so far indicate that ion exchange results in interlayer as well as intralayer incorporation. The formation of larger crystalline domains consisting of Ni/Fe/Co oxide can be excluded and a uniform statistical distribution of the ions can be assumed. To obtain complementary structural and electronic information, further characterization was performed by X-ray absorption spectroscopy (XAS) experiments. XAS is an element-specific method that can be applied to almost any material under nearly any environmental conditions and is not restricted to crystalline structures (like XRD) or specific electronic states (like NMR and EPR). This spectroscopic method has been successfully used for the analyses of birnessites by our groups before.[11,12,38,43,68] Accordingly,
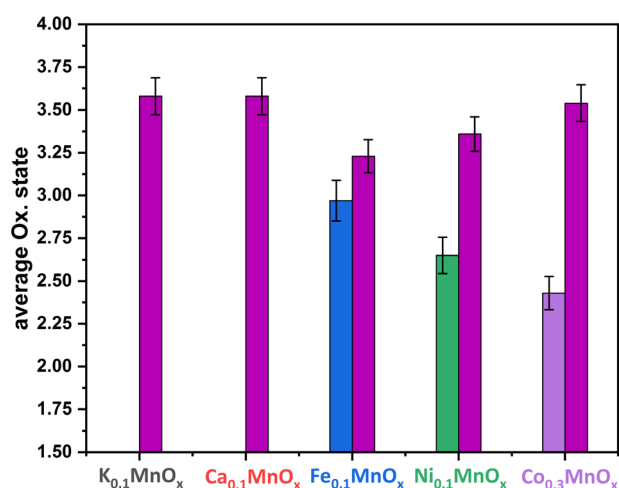
X-ray absorption near-edge structure (XANES) and extended X-ray absorption fine structure (EXAFS, Fig. 4) spectra at the Mn, Co, Ni and Fe K-edges were recorded for the as-prepared M_yMnO_x/CFP electrodes in order to determine the average oxidation states and local coordination environments of the different metal ions. The XANES and EXAFS spectra of all metals can be found in Fig. S19–S26 in the ESI.† In order to determine the average oxidation states of Mn, Co, Ni and Fe, the X-ray energy values at a normalized absorption of 0.5 of common reference compounds were used (see ESI Fig. S19–S25†). The mean oxidation states of the metals are visualized in Fig. 3, where it can be seen that the mean manganese oxidation states differ in a rather narrow range from +3.2 to +3.6.

Especially, the incorporation of Fe and Ni leads to a reduction of the Mn ions in comparison to $K_{0.1}MnO_x$/CFP, while the Mn oxidation state of the Ca and Co doped samples is very similar. On the other hand, an oxidation of Co and Ni occurs relative to the M^{2+} ions resulting in relative average oxidation states of +2.6 and +2.4, respectively, whereas Fe is always present in the form of Fe^{3+}. Thus, the number of Mn^{3+} ions in the birnessite structure is increased by Ni, Co and Fe-doping. This is an important finding, as Mn^{3+} sites are believed to be an essential active site feature in OER catalysis by MnO_x.[69–72]

Layered manganese oxides exhibit two different ion-exchange sites: metals can be incorporated into the interlayer space as well as into the layers themselves, while Co and Ni ions are able to fill in-layer vacancies within the $[MnO_6]$ octahedra of the sheets.[60,61,73,74] The latter, i.e. the incorporation into the oxide layer, was confirmed by Ni and Co EXAFS, as both spectra show Co–Mn/Ni–Mn scattering at ∼2.9 Å. This distance is close to the Mn–Mn distance (app. 2.85 Å) in the MnO_x layer and indicates that some Ni/Co ions are incorporated into the layers of $[MnO_6]$ octahedra. Such a distance can also be found for Fe, indicating that Fe ions can also become a part of the $[MnO_6]$ layers.[75] However, the doping of Ca^{2+} into the octahedral layers is unlikely as the ion has a much larger radius (∼114 pm) than Fe/Co/Ni/Mn cations (∼65–75 pm).[76]

Notably, a specific structural motif is obtained for Mn in the Fe doped samples. For the Ca, Co, and Ni doped electrodes, the local environment of the Mn ions is similar to two Mn–O distances at 1.84 and 1.95 Å and two Mn–M distances at roughly 2.9 and 3.4 Å, whereas three Mn–O shells at 1.84, 1.98 and 2.24 Å and two Mn–M shells at roughly 2.8 and 3.0 Å are present in the case of Fe (Fig. 4, S23, S24 and Table S4†). Moreover, the Mn–O or Mn–M shells sum up to populations (coordination number as determined by EXAFS simulations, Table S2†) of 4.8–5.1 (Mn–O) or 2.7–3.4 (Mn–M) for Ca, Co, and Ni, but for Fe they increase to 6.0 (Mn–O) and decrease to 2.4 (Mn–Fe). This suggests a lower degree of connectivity of the MnO_6 octahedra in the case of Fe and is most likely an effect of the lower Mn oxidation state.

The local environment of the doping ions, however, is different for all of them. Fe and Ni both exhibit M–O shells at circa 1.93 and 2.07 Å, but with quite different populations of 4.2/1.8 (Fe) or 2.1/3.4 (Ni). In contrast, Co has only one Co–O shell at 1.91 Å and the smallest overall first shell population of 4.6. The first M–M shell distance increases in the order Co

Fig. 3 Average oxidation states of Mn (plum), Fe (blue), Ni (green) and Co (purple) for M_yMnO_x/CFP electrodes. The oxidation states are derived from a linear fit of the data extracted at a normalized X-ray absorption intensity of 0.5 for reference compounds. See Fig. S19–S26 in the ESI† for more information. The error bars represent one standard deviation.
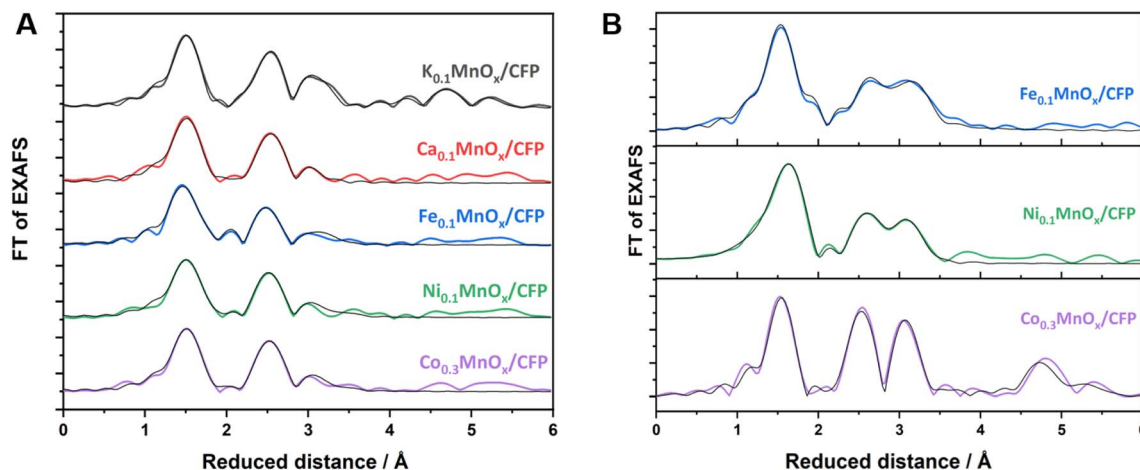
Fig. 4 FT of Mn (A) and Fe, Co, Ni (B) K-edge EXAFS spectra for M_yMnO_x/CFP electrodes. EXAFS simulations (parameters are given in Tables S2–S4 in the ESI†) are shown as black lines.

(2.85 Å) < Ni (2.90 Å) < Fe (2.95 Å), whereas the second M–M shell is very similar for all three (3.37–3.38 Å). The populations of all M–M shells, however, vary considerably between 1.3 and 4.6. By far the highest degree of ordering is obtained for Co, which, in addition to the highest M–M populations in the 3 Å regime, show pronounced Co–M shells at 4.99 and 5.46 Å. Accordingly, there is a tendency for higher ordering in the local Mn environment of the Co doped samples compared to Ca, Fe, and Ni. This higher order, which is also seen in the FT of the Co K-edge EXAFS spectrum, is most likely due to statistical reasons, as the number of $[CoO_6]$ octahedra is increased due to stoichiometry. The local formation of $(CoO_x)_n$ or CoO_xH_y building blocks next to incorporated $CoMnO_xH_y$ clusters or even local phases of pure CoO_x, however, can also not be totally excluded by the EXAFS data. In sum, the characterization methods used here indicate with a very high probability that there is a uniform, statistical distribution of Co ions in the birnessite backbone.

In conclusion, Ca/Fe/Co/Ni-doped MnO_x/CFP electrodes can be obtained *via* simple ion-exchange reactions, which is much faster in the case of Co^{2+}. All M_yMnO_x/CFP electrodes exhibit a layered, birnessite-type MnO_x structure. The doping of Fe/Ni cations leads to a reduction of the Mn ions, while Co and Ni are oxidized beyond the M^{2+} level. EXAFS revealed an incorporation of Fe/Co/Ni ions into the $[MnO_6]$ layers, whereas Ca^{2+} only occupies the interlayer space. Interestingly, the incorporation of Fe leads to a higher disorder within the MnO_x backbone, whereas for Co the opposite can be said.

2.2 Electrochemical characterization of M_yMnO_x/CFP electrodes

Next, we studied water oxidation electrocatalysis by M_yMnO_x/CFP in order to evaluate the influence of metal doping on the catalytic activities and stabilities. Three different pHs were chosen for this study: 1 M potassium phosphate buffer (pH 2.5 and 7.0, roughly corresponding to the first two pK_a values of phosphoric acid) or 1 M KOH (pH ~14.0).

All electrochemical measurements were manually corrected for ohmic losses at 85%, for which the electrolyte resistance R_u was determined by electrochemical impedance spectroscopy. Potentials were converted to the reversible hydrogen electrode (RHE) in order to obtain comparable values independent of the solvent pH.

Fig. 5 shows cyclic voltammograms in the anodic potential range from +1.0 to +1.8 V for M_yMnO_x/CFP electrodes operated at the three different pHs and show two distinct regions, which are typical of transition metal oxide electrodes immersed in aqueous electrolytes:

(1) from around 1.0–1.6 V, broad, unresolved pseudo-capacitive redox waves are discernible. As all electrodes are mainly composed of manganese, these are most likely attributable to $Mn^{3+} \rightleftharpoons Mn^{4+}$ transitions in combination with insertion/removal of H^+ or K^+ ions into/from the electrolytes to compensate for the differences in charge.[11,14,77] Nevertheless, a contribution of redox transitions from Co, Ni or Fe ions cannot be excluded, although no additional redox peaks, *e.g.* indicating a $Ni^{3+} \rightleftharpoons Ni^{4+}$ transition typically observable in NiO_x, are present;[78–81]

(2) an irreversible oxidation feature with a steep slope above potentials E of ~1.6 V for pH 2.5 and 7.0 and 1.5 V for pH 14.0 is indicative of the beginning of the water oxidation catalysis. The fact that this feature is visible for all electrodes at all tested pH values demonstrates their ability to catalyze the OER over the entire pH range. In general, earlier onset and higher current densities can be found for the electrodes operated under alkaline conditions. This is typical of first-row transition metal electrodes and has also been observed before.[14,24]

To further evaluate the electrochemical performances of M_yMnO_x/CFP electrodes, Tafel analyses were conducted using data generated from quasi-stationary stepwise chronoamperometry experiments as shown in Fig. S5.† In all cases, a nearly ideal linear dependence of $\log(j)$ *vs.* η was found for the current-density range from 0.1–10 mA cm^{-2}, indicating that the catalytic reaction is kinetically controlled under these conditions (*vs.* mass-transport limitations).
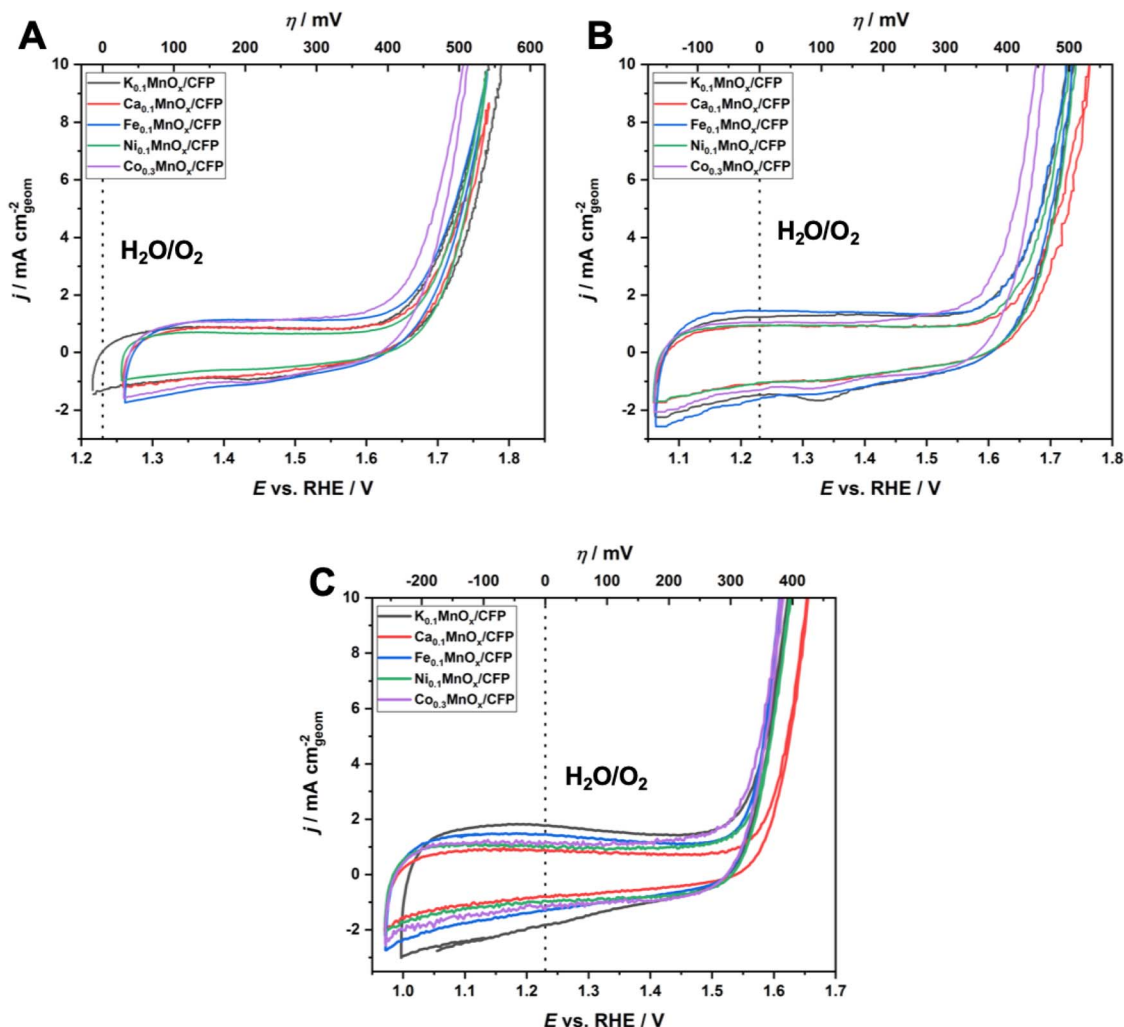
Fig. 5 Cyclic voltammograms for M_yMnO_x/CFP electrodes in 1 M KP$_i$-buffer at pH 2.5 (A) and pH 7.0 (B) and in 1 M KOH at pH 14.0 (C). In each case the 2nd CV cycle is plotted; scan rate: 20 mV s^{-1}. All shown traces are the average of at least three individual measurements.

For a comparison of the electrode activities, the overpotentials η needed to reach current densities of 1 and 5 mA cm^{-2}, extracted from the Tafel plots in Fig. S5,† are shown as bar graphs in Fig. 6A and are additionally listed in Table 1. All electrodes reached a benchmark current density of $j = 1$ mA cm^{-2} at overpotentials from 450–480 mV (pH 2.5), 420–450 mV (pH 7.0) and 310–360 mV (pH 14.0), respectively. Additionally, the difference $\Delta\eta$ between the overpotential needed by the $K_{0.1}MnO_x$/CFP electrode to reach 1 mA cm^{-2} and that needed by all other types of electrodes is shown in Fig. S6 in the ESI† (for values see Table 1). At pH 2.5, a minor activity enhancement can be found for the $Co_{0.3}MnO_x$/CFP electrode, while all other electrodes are worse than $K_{0.1}MnO_x$/CFP. For pH 7.0, the results are quite different: all tested electrodes show lower overpotentials of up to 30 mV indicating that at this pH the activity can be increased by metal doping. This is also the case at pH 14.0 for the Co- and Ni-doped electrodes, whereas Ca-doping leads to a pronounced deactivation.

Tafel slopes, listed in Table 1, were obtained by linear regression. For pH 2.5 and 7.0, the Tafel slopes are almost

constant and close to $2 \times 59 = 118$ mV dec^{-1}, which is typical of multi-step reactions, where the first oxidation is turnover-limiting.[82,83] Nevertheless, some minor differences can be discovered: slightly faster reaction kinetics are observed for doped electrodes as lower slopes than for the $K_{0.1}MnO_x$/CFP electrode are found.

One explanation for this behavior could be that the transfer of electrons can be increased by the incorporation of metal ions that increase the conductivity of the oxide backbone. Manganese oxides have a lower conductivity compared to Ni or Co oxides, a factor which has been shown in previous studies to limit the catalytic activity.[13–15] Nevertheless, a lowering of the Tafel slope is not in all cases accompanied by an improvement of the activity as shown by the ηs needed to reach a distinct reaction rate (see Table 1 and Fig. 6A).

For electrodes operated at pH 14.0, a change of the rate determining step can be assumed which is indicated by a pronounced decrease of the Tafel slope from ~120 mV dec^{-1} to values as low as 40 mV dec^{-1}, the latter being in line with multi-step reactions where the second step is potential-
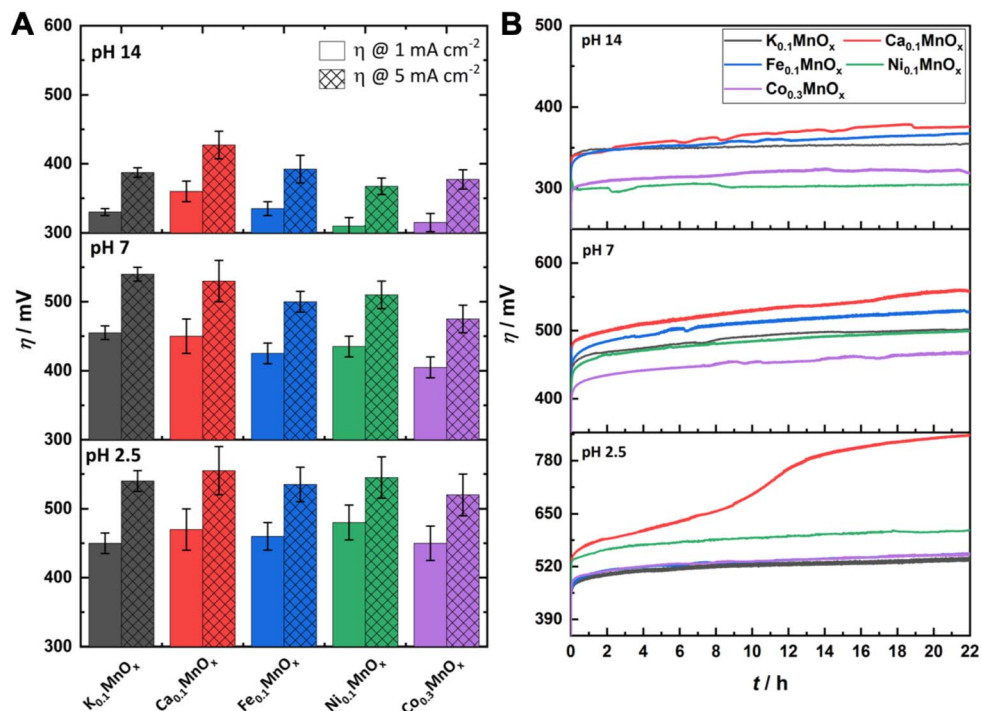
Fig. 6 (A) Overpotentials η needed to achieve WOC current-densities of 1 and 5 mA cm^{-2} at M$_y$MnO$_x$/CFP electrodes. Values are extracted from Tafel plots (see Fig. 5) generated from quasi-stationary stepwise chronoamperometry data. (B) η needed to maintain a current density of 2 mA cm^{-2} over a time of 22 h. All measurements were conducted in 1 M potassium phosphate buffer or 1 M potassium hydroxide solution at three different pH values (pH 2.5/7.0/14.0). All shown traces are the average of at least three individual measurements. The error bars represent one standard deviation.

independent.[82,84] Under alkaline conditions, the Ni- and Co-doped electrodes show the fastest reaction kinetics. Overall, the incorporation of Ni or Co has a positive effect on the activity of M$_y$MnO$_x$/CFP, whereas the effect of Ca or Fe is only small. The general trend described here for the Co-doped electrode Co$_{0.3}$-MnO$_x$/CFP can also be observed for an electrode, where the molar ratio of Mn : Co is only 1 : 0.1 (see Fig. S5†).

For a possible use as OER electrodes in technical applications, the long-term stabilities/activities of the anodes are of great importance. Therefore, the M$_y$MnO$_x$/CFP electrodes were also tested by chronopotentiometric measurements at a constant current density of 2 mA cm^{-2} over 22 h under the three pH conditions and the resulting η *vs.* t traces are shown in Fig. 6B.

For pH 2.5 the trend from the Tafel analyses is retained and no improvement of the electrode activity can be found. The behavior of Co$_{0.3}$MnO$_x$/CFP and Fe$_{0.1}$MnO$_x$/CFP is very similar to that of K$_{0.1}$MnO$_x$/CFP, whereas the Ni- and Ca-doped birnessites are less active. K, Ni, Co and Fe electrodes stay intact over the whole experiment and only a slight increase of η can be observed. In contrast, Ca-doping leads to an inactivation and a doubling of the overpotential after ~10 h. Although such an immense difference is only observable for pH 2.5, Ca$_{0.1}$MnO$_x$/CFP generally exhibits the worst long-term activity and stability of all tested electrodes at all pHs. This result was rather unexpected as Ca^{2+}-doping has been proven to enhance the catalytic activity of MnO$_x$ in experiments with Ce^{4+} (at pH ~ 2) and also thin-film MnO$_x$ electrodes operated at neutral pH. Furthermore,

Table 1 Tafel slopes, overpotentials η @ 1 and 5 mA cm^{-2}, difference $\Delta\eta$ between the overpotential needed to reach a current density of 1 mA cm^{-2} by the mature electrode (K$_{0.1}$MnO$_x$/CFP) and that needed by the other tested M$_y$MnO$_x$/CFP electrodes, overpotential needed to reach 2 mA cm^{-2} after 22 h of operation and redox active metal ions n(M)$_Q$ of M$_y$MnO$_x$/CFP electrodes for pH 2.5, 7.0 and 14.0

	Tafel slopes [mV dec^{-1}]			η @ 1 (5) mA cm^{-2} [mV]			$\Delta\eta$ [mV]			η @ 2 mA cm^{-2} after 22 h [mV]			n(M)$_Q$ [nmol cm^{-2}]		
	pH 2.5	pH 7.0	pH 14.0	pH 2.5	pH 7.0	pH 14.0	pH 2.5	pH 7.0	pH 14.0	pH 2.5	pH 7.0	pH 14.0	pH 2.5	pH 7.0	pH 14.0
K$_{0.1}$MnO$_x$	130	120	45	450 (540)	450 (540)	330 (360)	0	0	0	530	500	355	235	335	340
Ca$_{0.1}$MnO$_x$	115	120	60	470 (555)	450 (530)	360 (400)	+20	−5	+30	840	560	380	140	280	245
Fe$_{0.1}$MnO$_x$	110	110	50	460 (535)	425 (500)	335 (365)	+10	−30	+5	540	530	360	215	390	380
Ni$_{0.1}$MnO$_x$	110	105	40	480 (545)	435 (510)	310 (340)	+30	−20	−20	610	500	300	205	390	390
Co$_{0.3}$MnO$_x$	100	105	45	450 (520)	405 (475)	315 (350)	0	−50	−15	540	460	320	235	385	350

a Ca^{2+} cation is also an essential component of the OEC.[44,65,85,86] For synthetic $CaMnO_x$, the presence of Ca^{2+} leads to amorphization, which is accompanied by an increase of the surface area and assumed to be responsible for the higher catalytic activity. However, in $K_{0.1}MnO_x$/CFP, this increase in disorder is already achieved by the annealing step at 400 °C carried out in this study for all electrodes.[14] Furthermore, the additional Ca^{2+}-induced amorphization can have a destabilizing effect on the layered birnessite structure as for example shown by Suib and coworkers.[47] They concluded that this is caused by the larger ionic radius of Ca^{2+} causing stress on the Mn–O backbone leading to an easier breakdown of the ordered stacking of the layers. The combination of annealing and Ca^{2+} incorporation may here account for the destabilization of the structure and for the lower catalytic activity and stability of $Ca_{0.1}MnO_x$/CFP.

Under neutral conditions, Co-doping leads to a 40 mV improvement of the overpotential compared to all other electrodes, showing that the synergy of these metals, whose oxides belong to the most active earth-abundant OER catalysts under neutral conditions, is a promising approach.[15,87,88] However, no improvements can be found for Ni- and Fe-ion exchanged electrodes at pH 7.0.

At pH 14.0, the Ni- and Co-doped electrodes are able to catalyze the OER at overpotentials which are up to 60 mV lower compared to $K_{0.1}MnO_x$/CFP. Again, both NiO_x and CoO_x are themselves highly stable and active catalysts under alkaline conditions.[16–21] In the case of $Ni_{0.1}MnO_x$/CFP, an activation of the catalyst most likely caused by the formation of an active phase at the surface is observed during the experiment (see Fig. 7). Such a behavior is well known for Ni oxides and has been attributed to the incorporation of Fe impurities, which might also be accounted for here.[89]

Recently, our groups found a correlation between the catalytic activity and the number of manganese ions undergoing redox reactions during the catalytic cycle.[14] Such a correlation has also been found for Co-based electrodes.[90] In order to determine the influence of the cation doping on the molar amount of redox active metal ions, the cathodic scan of CVs recorded subsequent to the determination of the Tafel plots was integrated. As a result, the reduction charge Q is obtained, which divided by the Faraday constant F leads to the molar amount of redox active metal ions $n(M)_Q$ (see Table 1). From the $n(M)_Q$ data, it can be concluded that the number of redox active metal ions can be influenced by the incorporation of additional OER-active cations into the manganese oxide backbone. The previously observed activity trend is resembled here as the $Ca_{0.1}MnO_x$/CFP-electrode show the smallest $n(M)_Q$ values. As expected, a slight increase can be observed for pH 7.0 and pH 14.0, whereas a decrease for pH 2.5 is discernible for Fe-, Ni- and Co-doped electrodes compared to $K_{0.1}MnO_x$/CFP. For pH 2.5, the incorporated ions most likely do not participate in OER catalysis. Furthermore, the decrease (pH 2.5) or increase (pH 7/14) of the redox active sites for all doped electrodes additionally indicates that an electronic interaction between the Mn and M ions influencing their activity occurs. Thus, the increase in $n(M)_Q$ cannot be explained solely by the increased number of redox-active metal sites due to ion exchange. However, the
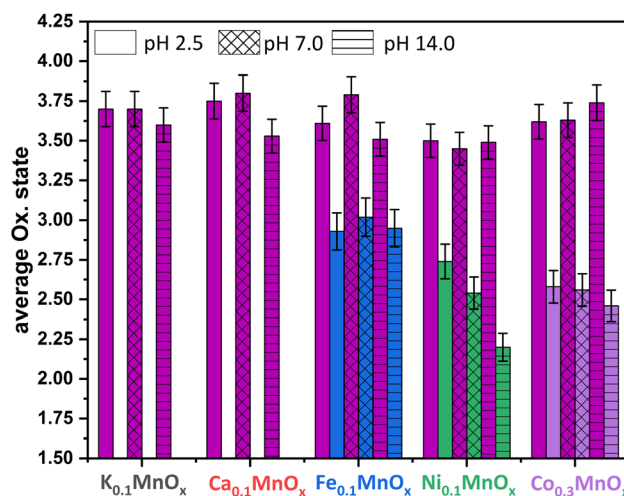

Fig. 7 Average oxidation states of Mn (plum), Fe (blue), Ni (green) and Co (purple) for M_yMnO_x/CFP electrodes after electrochemical operation under different pH conditions. The oxidation states are derived from a linear fit of the data extracted at a normalized X-ray absorption intensity of 0.5 for reference compounds. See also Fig. S19–S26 in the ESI† for more information. The error bars represent one standard deviation.

extent of this interaction and its influence on the activity cannot be determined. Hence, the determination of $n(M)_Q$ is a very useful instrument to compare the activities of MnO_x or other metal oxide electrodes.

To further evaluate whether the higher activity, especially of the Co-doped electrode, is only due to the higher loading of OER-active cations, the long-term stability of a $Co_{0.3}MnO_x$/CFP electrode during constant application of $j = 2$ mA cm^{-2} is compared to that of a $K_{0.1}MnO_x$/CFP electrode exhibiting nearly an identical number of Mn/M ions ($n(Co + Mn)_{AAS} = 3.9$ μmol cm^{-2} *vs.* $n(Mn)_{AAS} = 4.0$ μmol cm^{-2}, Fig. S9†). Interestingly, the Co-doped electrode needed an app. 50 mV lower overpotential after 24 h of operation in 1 M KP_i at pH 7.0. Consequently, the higher activity of $Co_{0.3}MnO_x$/CFP electrodes cannot simply be explained by the increase in the total number of OER active metal sites. Thus, a synergistic effect between the incorporated ions and manganese seems more likely.

In conclusion, the electrochemical activity and stability of $K_{0.1}MnO_x$/CFP electrodes can be improved by the incorporation of Fe, Ni, and Co cations by an ion-exchange reaction. The incorporation has a positive influence on the electrode kinetics, the overall activities and the number of active redox sites. However, the effect is not the same for all ions tested and additionally depends on the pH at which the electrochemical tests are carried out. Thus, large improvements are especially found for Co under neutral and Co and Ni under strongly alkaline conditions.

2.3 *Post operando* characterization of electrodes

In order to determine morphological or structural changes that could explain the different WOC behavior of the M_yMnO_x/CFP catalysts, *ex situ post operando* studies after 22 h of continuous

operation were conducted at the same three pH values as studied before.

First, possible changes of the surface morphologies due to long-term electrochemical water oxidation were examined by SEM (Fig. S8†). Only minor changes are visible for the electrodes operated under different pH conditions, indicating that the basic birnessite structure of the parent M_yMnO_x/CFP electrodes is retained. Only for the electrodes operated at pH 2.5, a broadening of the threads building a sponge-like structure can be detected, which has also been observed before for $K_{0.1}MnO_x$/CFP electrodes.[14]

To evaluate whether the electrochemical treatment led to a leaching of the incorporated metal ions from the manganese oxide backbone, the atomic ratios were determined by EDX. From Fig. S10–S14,† it can be seen that even under acidic conditions no leaching occurred. This points towards a reasonable stabilization especially of Co and Ni ions by incorporation into the birnessite backbone as these oxides normally dissolve in the acid according to their Pourbaix diagrams.[91] Additionally, an incorporation of potassium (atomic ratio of $K:Mn \sim 0.1:1$) and phosphate (atomic ratio of $P:Mn \sim 0.1:1$) ions from the electrolyte can be observed.

Powder XRD patterns (Fig. S15†) show no additional reflexes compared to the electrodes after preparation, which confirms the SEM findings and additionally shows that the carbon support remains intact. ATR-IR-spectra reveal no additional bands for the M_yMnO_x/CFP electrodes that have been exposed to anodic potentials, except for electrodes operated in phosphate buffers (pH 2.5 and pH 7.0; Fig. S16†). Here, two broad features between 1150 and 950 cm^{-1} can be observed, which have been observed before and are most likely attributable to the incorporated phosphate ions ($H_nPO_4^{(3-n)-}$).[14] Such features are not visible for the electrodes operated in 1 M KOH, confirming the interpretation as interactions between the phosphate anions and the manganese oxide.

All results obtained by these mainly bulk sensitive measurement techniques are typical of amorphous birnessites. In order to reveal details on the chemical states and the local atomic environment of the metal centers, synchrotron-based XAS studies were again carried out.

The XAS-data based oxidation states for Mn, Fe, Ni and Co are visualized in Fig. 7. The average manganese oxidation states vary within a rather narrow range from +3.4 to +3.8 and are generally higher compared to their *pre operando* values (see Fig. 3). This confirms our interpretation of the CV that the Mn ions are oxidized, a fact that was repeatedly observed before.[11–14] However, the highest oxidation states for Mn are generally found for the least active catalysts. This supports the importance of stable Mn^{3+} states within the mixed valent MnO_x-based OER catalysts proposed by several authors.[46,69,70,92]

No change of the average oxidation state of the Fe ions is visible pointing to relatively high inertness of the +III state within the manganese oxide framework. Nevertheless, only *in situ* XAS or Mössbauer spectroscopy measurements could show whether other oxidation states, *e.g.* Fe^{4+}, are also present at catalytic potentials, as these have recently been found for Ni–Fe oxyhydroxides,[10,93] and see also ref. 94.

The likely contribution of Ni to the higher activity under neutral and especially under alkaline conditions can be recognized by a lowering of the average oxidation state of the Ni ions from ~ 2.6 (as-prepared, pH 2.5) *via* ~ 2.5 (pH 7.0) to ~ 2.2 for pH 14.0. This eventually leads to the assumption that Ni^{2+} is, besides Mn, also an OER active species in $Ni_{0.1}MnO_x$/CFP under alkaline conditions. In addition, the lowering of the Ni oxidation state at pH 14.0 might be the reason for the lowering of η (catalyst activation) in the first minutes of the chronopotentiometry measurements discussed above. A stabilization of Ni in lower oxidation states than +IV (the usually dominant Ni oxidation state in Ni-only oxides) has recently been observed for Fe containing Ni oxides.[81,95]

For the incorporated Co ions, a slight oxidation after operation in 1 M phosphate buffers of pH 2.5 and 7.0 can be observed, whereas the average oxidation state is retained after operation at pH 14.0. Fractional oxidation states of $\sim +2.6$ have also been found for phosphate containing cobalt oxide in its resting state.[96,97] Furthermore, Co oxide OER catalysts are highly dynamic systems able to reversibly switch between the oxidation states +2/+3/+4 during catalysis.[96,97] A contribution of the Co ions to the OER activity in $Co_{0.3}MnO_x$/CFP seems therefore likely, but again has to be proven by *in situ* techniques.

A detailed look at the XAS data in Fig. S19–S26† reveals that the M–O and M–M distances are well conserved for all metals (Mn, Fe, Co, and Ni) under all conditions (as prepared, operated at pH 2.5, 7.0, and 14.0). Only above 3 Å changes larger than 0.1 Å appear. Shell populations typically vary in the range of roughly ± 0.3 for the first ligand sphere, ± 0.5 for the second and ± 0.7 for far distant shells. Considering this, a tendency for higher M–M shell populations after operation can be detected for all metal types except Fe, suggesting a higher degree of ordering in most cases.

In conclusion, no major structural changes of the basic birnessite phase as well as the local coordination environments of the tested metal-doped electrodes were uncovered by ATR-IR, XRD, XAS, EDX and SEM measurements after long-term WOC operation at pH 2.5/7.0/14.0. Therefore, the studied anodes can be characterized as stable and catalytically active OER anodes over a wide pH range. EDX measurements revealed that no leaching occurred during operation. Furthermore, it can be concluded that the increase of the activity and stability, especially for Ni- and Co-doped electrodes, is due to a synergistic effect between the manganese oxide backbone and the incorporated metal ions.

2.4 Comparison with other state-of-the-art OER catalysts

For a better comparison of the metal doped manganese oxide catalysts, we immobilized IrO_x, CoP_i and $FeNiO_x$ on CFP following well-established literature procedures.[87,98–101] To confirm the deposition, the SEM micrographs of the metal oxide coated CFP can be found in Fig. S14† and again carbon supports uniformly covered by the catalyst layers are visible.

As before for M_yMnO_x/CFP, the electrocatalytic OER activities and stabilities were evaluated by Tafel analyses (Fig. S17†) and long-term chronopotentiometry measurements (Fig. S18†).
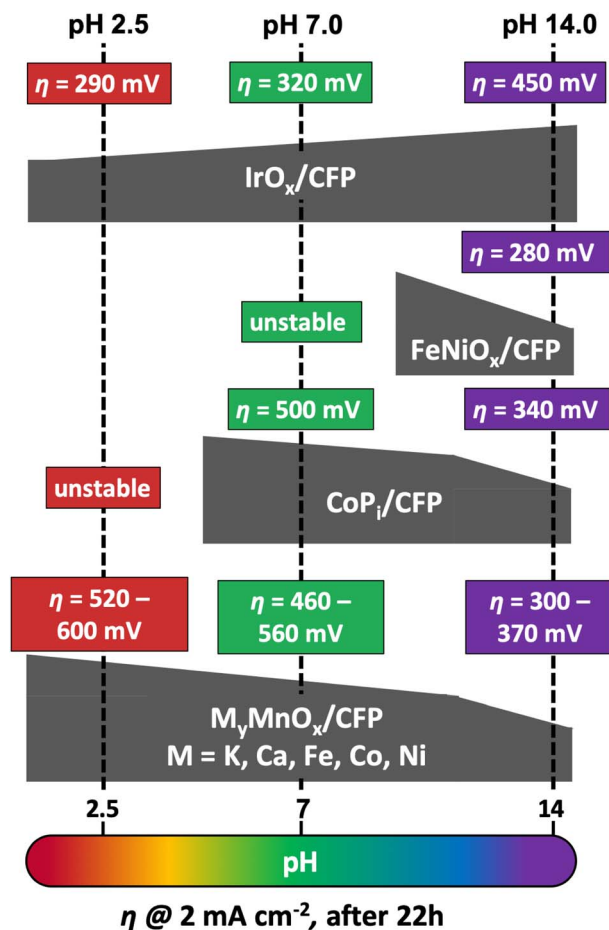
Fig. 8 Comparison of overpotentials η needed to reach 2 mA cm^{-2} after 22 h of operation at pH 2.5, 7.0 or 14.0 by different MO$_x$/CFP electrodes.

electrodes in acidic media, highlighting the remarkable catalytic abilities of iridium oxides at low pH.[16,102] Nevertheless, the manganese oxide-based electrodes are the only stable alternative among the tested electrodes under acidic conditions. Furthermore, the activity of the M$_y$MnO$_x$/CFP electrodes is still very good compared to other earth-abundant metal oxide catalyst systems and ranks amongst the best that have so far been reported.[15,22,24,54,102–105]

At pH 7.0, IrO$_x$/CFP still exhibits the highest activity and stability, whereas FeNi oxide remains unstable. The behavior of CoP$_i$/CFP, one of the most active earth-abundant catalysts under neutral conditions, is quite similar to that of K$_{0.1}$MnO$_x$/CFP, showing that both metal oxides are nearly equally active. However, the mixture of Co and Mn reaches higher activities, again indicating that the synergy of these two elements can be a promising approach to yield even more active OER electrocatalysts.

Interestingly, under alkaline conditions, IrO$_x$ behaves contrary to the other transition metal oxides studied, as a fast increase of η in the first hours of the experiments was observed as reported before.[106–108] On the other hand, CoP$_i$ and FeNiO$_x$ behave like MnO$_x$ and show higher stabilities and activities at pH 14.0.[14] The FeNiO$_x$/CFP electrodes show remarkable activities similar to the Ni-doped MnO$_x$ electrode at pH 14.0, under the tested catalyst systems. Hence, the M$_y$MnO$_x$/CFP electrodes and especially the Ni$_{0.1}$MnO$_x$/CFP electrode can easily compete with the CoP$_i$ and the IrO$_x$ electrode as well as with other Mn-based catalysts.[15,54,103,109] However, the exceptional activities of FeNiO$_x$ at pH $\geq$ 13 and of that reported in the literature for operation in strongly alkaline media are so far out of reach for MnO$_x$-based electrocatalysts.[17,80,110,111]

3 Conclusions

In this study, we presented the facile preparation of metal-doped (Co, Ca, Ni, and Fe) layered manganese oxides coated on carbon fiber paper substrates for electrocatalytic water oxidation. The preparation was based on a well-established, easily scalable redox-deposition approach followed by an ion-exchange reaction using metal nitrate solutions. The additional metal ions were incorporated in both the interlayer space and the MnO$_6$ sheets and had only a minor effect on the morphology and the structure of the basic birnessite backbone. XAS measurements, on the other hand, showed that the oxidation states of manganese can be lowered by ion exchange, leading to the introduction of a larger number of WOC-active

The overpotentials needed after 22 h of constant operation are schematically presented in Fig. 8 in comparison to the results obtained for the mixed metal oxide electrodes. Overpotentials, Tafel slopes and long-term stability parameters are listed in Table 2.

As predicted from the Pourbaix diagram, FeNiO$_x$/CFP and CoP$_i$/CFP electrodes are unstable at pH 2.5, leading to a complete dissolution of the catalyst layer from the carbon support within minutes of operation.[91] On the other hand, IrO$_x$/CFP exhibits good stability and overpotentials, which are more than 200 mV lower compared to the best M$_y$MnO$_x$/CFP

Table 2 Tafel slopes, overpotentials η @ 1 and 5 mA cm^{-2} and overpotential needed to reach 2 mA cm^{-2} after 22 h of operation of MO$_x$/CFP electrodes for pH 2.5, 7.0 and 14.0. For all entries which are marked by * it was not possible to receive values due to a fast corrosion of the catalyst, leading to a too early termination of the electrochemical experiment under the used pH conditions

	Tafel slope [mV dec^{-1}]			η @ 1 (5) mA cm^{-2} [mV]			η @ 2 mA cm^{-2} after 24 h [mV]		
	pH 2.5	pH 7.0	pH 14.0	pH 2.5	pH 7.0	pH 14.0	pH 2.5	pH 7.0	pH 14.0
IrO$_x$	80	70	60	260 (300)	230 (280)	250 (290)	290	320	450
CoP$_i$	*	120	60	*	420 (510)	310 (360)	*	500	340
NiFeO$_x$	*	*	40	*	*	280 (310)	*	*	280

Mn^{3+} ions. Overall, Fe doped MnO_x layers exhibited the lowest average manganese oxidation state.

Electrochemical measurements revealed that M_yMnO_x/CFP are efficient and stable anodes for electrocatalytic water oxidation over nearly the entire aqueous pH regime (pH 2.5–14.0). Differences were especially found for Co- and Ni-doped electrodes, whose WOC activities and stabilities were clearly improved compared to the undoped $K_{0.1}MnO_x$/CFP electrode. The reasons for these improvements might be due to a synergistic effect between the OER-active metal centers, a higher electrical conductivity and/or better charge transfer properties. The exact causes have to be addressed in future studies, for example by *in situ* XAS- or four-point probe resistivity measurements.

Ex situ post operando spectroscopy analysis confirmed the stability of M_yMnO_x electrodes. Slight changes of the average Mn, Co and Ni oxidation states were observed, indicating the participation of these elements in the catalytic process. However, a clear proof (for example by *in situ* XAS measurements) has so far been missing, but will be tackled in subsequent studies.

Overall, (doped) manganese oxides stand out as WOC materials over a wide pH range, especially due to their universal applicability. In addition, under intermediate pH conditions, together with cobalt oxides, they show one of the highest activities of earth-abundant catalysts. They thus represent a promising catalyst alternative at pHs below 7 with possible applications like artificial leaves or photoelectrochemical cells (PECs), which are normally operated at intermediate pHs and at relatively low current densities ($j \sim 10$ mA cm^{-2}).[112,113] Similarly, microbial electrosynthesis cells (MESCs) might be an alternative application for MnO_x anodes.

4 Experimental section

4.1 Materials

Graphitized carbon fibre paper (CFP, TGP-H-60) was purchased from Toray Carbon Inc., cut into pieces of 1×2 cm^2 and pre-treated by sonication for 15 min each in 0.1 M HNO$_3$, ethanol and water, respectively. Please see the ESI† for further details concerning the materials used for this study.

4.2 Preparation of M_yMnO_x/CFP electrodes

The preparation of $K_{0.1}MnO_x$/CFP electrodes using the *in situ* redox reaction between permanganate and carbon has been described in detail elsewhere.[13,14] In short, 2.5 mL of HNO$_3$ (69%) was added to a beaker containing a KMnO$_4$ solution (0.1 M, 100 mL) and the strongly acidic mixture (pH 0.4) was then heated to 70 °C. Subsequently, four pre-treated pieces of CFP were dipped into the slowly stirred solution simultaneously for 90 min. To ensure that only 1 cm^2 of the carbon material was exposed to the solution, the rest of the area was covered with adhesive tape (tesafilm®, "matt-unsichtbar", thickness ~ 70 μm). The electrodes were then taken out of the KMnO$_4$ solution, washed thoroughly with water and dried in air at 60 °C for 1 h. In order to obtain ion exchanged M_yMnO_x/CFP electrodes, the parent $K_{0.1}MnO_x$/CFP electrodes were then dipped into a beaker containing a solution of

1 M $M^{2+/3+}(NO_3)_{2/3}$ (with M = Fe^{3+}, Ni^{2+} or Ca^{2+}) or 0.1 M $Co^{2+}(NO_3)_2$. Ion exchange was carried out for different times (15 min to 24 h) in order to obtain various numbers of incorporated metal ions. Finally, the M_yMnO_x/CFP electrodes were washed with water, dried in air at 60 °C for 1 h and calcined in a muffle furnace in air at a temperature of 400 °C for 1 h.

4.3 Preparation of MO_x/CFP electrodes

For a better comparison with current state-of-the-art OER catalysts, IrO_x, $FeNiO_x$ and CoP_i were electrodeposited on CFP following published procedures:

IrO_x/CFP was prepared *via* a method developed by Petit *et al.*:[98] 2 mM K_3IrCl_6 was dissolved in water and 15 mM oxalic acid and 100 mM K_2CO_3 were added (pH 10.5). This solution was then stirred for 10 days at room temperature until the color turned from pale yellow to light blue. During the aging time, it is assumed that an $[Ir(C_2O_4)(OH)_4]^{2-}$ complex is formed, which can be anodically electrodeposited on CFP.[99] The electrodeposition was conducted in a typical three electrode setup (see below) by applying a constant current density of 350 μA cm^{-2} until a charge $Q = 5$ mC cm^{-2} had passed through the electrode.

FeNiO$_x$/CFP was prepared following a synthesis route developed by Lu *et al.*:[100] 3 mM $Fe^{3+}(NO_3)_3 \cdot 9H_2O$ and 3 mM $Ni^{2+}(NO_3)_2 \cdot 6H_2O$ were dissolved in water. This mixture was then used to cathodically deposit mixed $NiFeO_x$ on CFP in a typical three electrode setup (see below). The electrodeposition was carried out by applying a constant potential of -1.0 V *vs.* Ag/AgCl for 300 s. It is assumed that the electrodeposition occurs *via* the reduction of NO_3^- at the electrode surface leading to the generation of hydroxides, which then react with Fe^{3+} and Ni^{2+} to form bimetallic hydroxide deposits on the surface.

CoP_i/CFP was prepared following a well-established route developed by Nocera and co-workers:[87,101] 0.5 mM $Co^{2+}(NO_3)_2 \cdot 6H_2O$ was dissolved in a 0.1 M potassium phosphate buffer (pH 7.0). The electrodeposition of CoP_i on CFP was conducted in a typical three electrode setup by applying a constant potential of 1.71 V *vs.* RHE until a charge $Q = 40$ C cm^{-2} passed through the WE.

In order to be able to compare the activities per geometric electrode area of each type of catalyst, we tried to deposit approximately the same mass loading on the conductive substrate.

4.4 Instrumental methods

Details of the instrumentation and measurement conditions used to record vibrational spectra (ATR-FT-IR), electron micrographs (SEM), energy dispersive X-ray analyses (EDX), and X-ray absorption spectra (XAS) and for the determination of metal ion fractions by flame atomic absorption spectroscopy (fAAS) are provided in the ESI.†

4.5 General electrochemical details

All electrochemical experiments were conducted in a typical three-electrode setup using a BioLogic VSP potentiostat/galvanostat with an integrated module for electrochemical impedance spectroscopy (EIS). The electrochemical cell (volume 100 mL) typically consisted of an Ag/AgCl reference electrode

(Metrohm, 3 M KCl, +0.207 V *vs.* NHE at 25 °C), a Pt rod as the counter electrode separated by a porous glass frit (Metrohm, diameter $\sim$ 2 mm) and M_yMnO_x/CFP as the working electrodes (WE). All measurements were conducted in 50 mL of the respective air-saturated electrolyte (1 M potassium phosphate buffer at pH 2.5/7.0 or 1 M KOH at pH 14.0) at ambient temperature ($\sim$23 °C). WE potentials were converted to the RHE according to eqn (1).

$$E_{RHE} = E_{Ag/AgCl} + 0.207 + 0.059\text{pH (in V)} \tag{1}$$

To evaluate the electrocatalytic behaviour of the M_yMnO_x/CFP anodes for water oxidation in different electrolytes, a multi-step protocol consisting of the determination of the uncompensated resistance R_u (by EIS) followed by "staircase" chronoamperometry measurements (CA, for the determination of Tafel plots) and terminated by cyclic voltammetry sweeps (CV) over a wide potential range was used (see the ESI for details†). To minimize the possibility of mass transport limitations and the formation of a pH gradient in the pores of the catalyst, the solutions were stirred at a constant speed (600 rpm) during the CA measurements. In staircase CA protocols, potentials were held constant for 5 min at each step in order to exclude a large contribution of the capacitive current to the overall current density. The average current density over the last 30 s of each step was then used for the Tafel analyses. To evaluate the long-term stability of M_yMnO_x/CFP under different electrolyte conditions, chronopotentiometry measurements (CP) at current densities of 2 mA cm^{-2} were performed for a duration of 24 h. All CA, CP and CV measurements were *iR* corrected at 85%.

Conflicts of interest

There are no conflicts to declare.

Acknowledgements

Notes and references

1 D. G. Nocera and N. S. Lewis, *Proc. Natl. Acad. Sci. U. S. A.*, 2006, **103**, 15729–15735.

2 R. Schlögl, *ChemSusChem*, 2010, **3**, 209–222.

3 N. Armaroli and V. Balzani, *Angew. Chem., Int. Ed.*, 2007, **46**, 52–66.

4 M. Carmo, D. L. Fritz, J. Mergel and D. Stolten, *Int. J. Hydrogen Energy*, 2013, **38**, 4901–4934.

5 H. Dau, C. Limberg, T. Reier, M. Risch, S. Roggan and P. Strasser, *ChemCatChem*, 2010, **2**, 724–761.

6 G. P. Gardner, Y. B. Go, D. M. Robinson, P. F. Smith, J. Hadermann, A. Abakumov, M. Greenblatt and G. C. Dismukes, *Angew. Chem., Int. Ed.*, 2012, **51**, 1616–1619.

7 M. Dincǎ, Y. Surendranath and D. G. Nocera, *Proc. Natl. Acad. Sci. U. S. A.*, 2010, **107**, 10337–10341.

8 D. K. Bediako, B. Lassalle-Kaiser, Y. Surendranath, J. Yano, V. K. Yachandra and D. G. Nocera, *J. Am. Chem. Soc.*, 2012, **134**, 6801–6809.

9 Y. Wu, M. Chen, Y. Han, H. Luo, X. Su, M. T. Zhang, X. Lin, J. Sun, L. Wang, L. Deng, W. Zhang and R. Cao, *Angew. Chem., Int. Ed.*, 2015, **54**, 4870–4875.

10 J. Y. C. Chen, L. Dang, H. Liang, W. Bi, J. B. Gerken, S. Jin, E. E. Alp and S. S. Stahl, *J. Am. Chem. Soc.*, 2015, **137**, 15090–15093.

11 I. Zaharieva, P. Chernev, M. Risch, K. Klingan, M. Kohlhoff, A. Fischer and H. Dau, *Energy Environ. Sci.*, 2012, **5**, 7081–7089.

12 S. Y. Lee, D. González-Flores, J. Ohms, T. Trost, H. Dau, I. Zaharieva and P. Kurz, *ChemSusChem*, 2014, **7**, 3442–3451.

13 J. Melder, W. L. Kwong, D. Shevela, J. Messinger and P. Kurz, *ChemSusChem*, 2017, **10**, 4491–4502.

14 J. Melder, S. Mebs, P. A. Heizmann, R. Lang, H. Dau and P. Kurz, *J. Mater. Chem. A*, 2019, **7**, 25333–25346.

15 J. Melder, P. Bogdanoff, I. Zaharieva, S. Fiechter, H. Dau and P. Kurz, *Z. Phys. Chem.*, 2020, **234**(5), 925–978.

16 N.-T. Suen, S.-F. Hung, Q. Quan, N. Zhang, Y.-J. Xu and H. M. Chen, *Chem. Soc. Rev.*, 2017, **46**, 337–365.

17 E. L. Miller and R. L. Rocheleau, *J. Electrochem. Soc.*, 1997, **144**, 3072.

18 A. Ursua, L. Gandia and P. Sanchis, *Proc. IEEE*, 2012, **100**, 410–426.

19 A. M. Smith, L. Trotochaud, M. S. Burke and S. W. Boettcher, *Chem. Commun.*, 2015, **51**, 5261–5263.

20 B. M. Hunter, J. D. Blakemore, M. Deimund, H. B. Gray, J. R. Winkler and A. M. Müller, *J. Am. Chem. Soc.*, 2014, **136**, 13118–13121.

21 S. Loos, I. Zaharieva, P. Chernev, A. Lißner and H. Dau, *ChemSusChem*, 2019, **12**, 1966–1976.

22 K. Sun, I. A. Moreno-Hernandez, W. C. Schmidt, X. Zhou, J. C. Crompton, R. Liu, F. H. Saadi, Y. Chen, K. M. Papadantonakis and N. S. Lewis, *Energy Environ. Sci.*, 2017, **10**, 987–1002.

23 A. Minguzzi, F.-R. F. Fan, A. Vertova, S. Rondinini and A. J. Bard, *Chem. Sci.*, 2012, **3**, 217.

24 C. C. L. McCrory, S. Jung, I. M. Ferrer, S. Chatman, J. C. Peters and T. F. Jaramillo, *J. Am. Chem. Soc.*, 2015, **137**, 4347–4357.

25 C. C. L. McCrory, S. Jung, J. C. Peters and T. F. Jaramillo, *J. Am. Chem. Soc.*, 2013, **135**, 16977–16987.

26 P. C. K. Vesborg and T. F. Jaramillo, *RSC Adv.*, 2012, **2**, 7933–7947.

27 R. E. Smalley, *MRS Bull.*, 2005, **30**, 412–417.

28 K. Rabaey and R. A. Rozendal, *Nat. Rev. Microbiol.*, 2010, **8**, 706–716.

29 R. Ganigué, S. Puig, P. Batlle-Vilanova, M. D. Balaguer, J. Colprim, M. Mikkelsen, M. Jørgensen, F. C. Krebs, R. S. Haszeldine, K. Rabaey, R. A. Rozendal, K. P. Nevin, T. L. Woodard, A. E. Franks, Z. M. Summers, D. R. Lovley, C. W. Marshall, D. E. Ross, E. B. Fichot, R. S. Norman, H. D. May, C. W. Marshall, D. E. Ross, E. B. Fichot, R. S. Norman, H. D. May, M. Sharma, N. Aryal, P. M. Sarma, K. Vanbroekhoven, B. Lal, X. D. Benetton, D. Pant, K. J. J. Steinbusch, H. V. M. Hamelers, J. D. Schaap, C. Kampman, C. J. N. Buisman, M. C. A. A. V. Eerten-Jansen, A. T. Heijne, T. I. M. Grootscholten, K. J. J. Steinbusch, T. H. J. A. Sleutels, H. V. M. Hamelers, C. J. N. Buisman, M. Dwidar, J.-Y. Park, R. J. Mitchell, B.-I. Sang, P. Sánchez, R. Ganigue, L. Bañeras, J. Colprim, J. Daniell, M. Köpke, S. D. Simpson, A. S. Gössner, F. Picardal, R. S. Tanner, H. L. Drake, R. K. Thauer, K. Jungermann, K. Decker, P. P. H. Pi, M. T. Agler, B. A. Wrenn, S. H. Zinder, L. T. Angenent, P. Batlle-Vilanova, S. Puig, R. Gonzalez-Olmos, A. Vilajeliu-Pons, L. Bañeras, M. D. Balaguer, J. Colprim, A. W. Jeremiasse, H. V. M. Hamelers, C. J. N. Buisman, M. C. A. A. V. Eerten-jansen, A. T. Heijne, C. J. N. Buisman, H. V. M. Hamelers, I. Bechthold, K. Bretz, S. Kabasci, R. Kopitzky, A. Springer, S. J. Andersen, T. Hennebel, S. Gildemyn, M. Coma, J. Desloover, J. Berton, J. Tsukamoto, C. V. Stevens, K. Rabaey, R. S. Tanner, L. M. Miller and D. Yang, *Chem. Commun.*, 2015, **51**, 3235–3238.

30 K. P. Nevin, T. L. Woodard and A. E. Franks, *mBio*, 2010, **1**, e00103–e00110.

31 N. Aryal, F. Ammam, S. A. Patil and D. Pant, *Green Chem.*, 2017, 5748–5760.

32 J. Kibsgaard and I. Chorkendorff, *Nat. Energy*, 2019, 430–433.

33 A. Marshall, S. Sunde, M. Tsypkin and R. Tunold, *Int. J. Hydrogen Energy*, 2007, **32**, 2320–2324.

34 N. Cox, D. A. Pantazis, F. Neese and W. Lubitz, *Acc. Chem. Res.*, 2013, **46**, 1588–1596.

35 J. Barber, *Chem. Soc. Rev.*, 2009, **38**, 185–196.

36 H. Dau and I. Zaharieva, *Acc. Chem. Res.*, 2009, **42**, 1861–1870.

37 C. E. Frey and P. Kurz, *Chem.–Eur. J.*, 2015, **21**, 14958–14968.

38 I. Zaharieva, M. M. Najafpour, M. Wiechen, M. Haumann, P. Kurz and H. Dau, *Energy Environ. Sci.*, 2011, **4**, 2400–2408.

39 R. K. Hocking, R. Brimblecombe, L.-Y. Chang, A. Singh, M. H. Cheah, C. Glover, W. H. Casey and L. Spiccia, *Nat. Chem.*, 2011, **3**, 461–466.

40 A. Ramírez, D. Friedrich, M. Kunst and S. Fiechter, *Chem. Phys. Lett.*, 2013, **568–569**, 157–160.

41 Y. Meng, W. Song, H. Huang, Z. Ren, S.-Y. Chen and S. L. Suib, *J. Am. Chem. Soc.*, 2014, **136**, 11452–11464.

42 D. M. Robinson, Y. B. Go, M. Mui, G. Gardner, Z. Zhang, D. Mastrogiovanni, E. Garfunkel, J. Li, M. Greenblatt and G. C. Dismukes, *J. Am. Chem. Soc.*, 2013, **135**, 3494–3501.

43 M. Wiechen, I. Zaharieva, H. Dau and P. Kurz, *Chem. Sci.*, 2012, **3**, 2330.

44 D. González-Flores, I. Zaharieva, J. Heidkamp, P. Chernev, E. Martínez-Moreno, C. Pasquini, M. R. Mohammadi, K. Klingan, U. Gernet, A. Fischer and H. Dau, *ChemSusChem*, 2016, **9**, 379–387.

45 J. E. Post, *Proc. Natl. Acad. Sci. U. S. A.*, 1999, **96**, 3447–3454.

46 A. Li, H. Ooka, N. Bonnet, T. Hayashi, Y. Sun, Q. Jiang, C. Li, H. Han and R. Nakamura, *Angew. Chem., Int. Ed.*, 2019, **58**, 5054–5058.

47 J. Cai, J. Liu and S. L. Suib, *Chem. Mater.*, 2002, **14**, 2071–2077.

48 I. G. McKendry, A. C. Thenuwara, S. L. Shumlas, H. Peng, Y. V. Aulin, P. R. Chinnam, E. Borguet, D. R. Strongin and M. J. Zdilla, *Inorg. Chem.*, 2018, **57**, 557–564.

49 I. G. Mckendry, L. J. Mohamad, A. C. Thenuwara, T. Marshall, E. Borguet, D. R. Strongin and M. J. Zdilla, *ACS Energy Lett.*, 2018, **3**, 2280–2285.

50 A. C. Thenuwara, S. L. Shumlas, N. H. Attanayake, Y. V. Aulin, I. G. Mckendry, Q. Qiao, Y. Zhu, E. Borguet, M. J. Zdilla and D. R. Strongin, *ACS Catal.*, 2016, **6**, 7739–7743.

51 B. Dutta, S. March, L. Achola, S. Sahoo, J. He, A. Amin Shirazi, Y. Wu, S. Poges, S. P. Alpay and S. L. Suib, *Green Chem.*, 2018, **20**, 3180–3185.

52 S. Biswas, B. Dutta, A. Mannodi-Kanakkithodi, R. Clarke, W. Song, R. Ramprasad and S. L. Suib, *Chem. Commun.*, 2017, **53**, 11751.

53 X. Li, T. Lunkenbein, V. Pfeifer, M. Jastak, P. K. Nielsen, F. Girgsdies, A. Knop-Gericke, F. Rosowski, R. Schlögl and A. Trunschke, *Angew. Chem., Int. Ed.*, 2016, **55**, 4092–4096.

54 M. Huynh, T. Ozel, C. Liu, E. C. Lau and D. G. Nocera, *Chem. Sci.*, 2017, **8**, 4779–4794.

55 K. Fujimoto, T. Okada and M. Nakayama, *J. Phys. Chem. C*, 2018, **122**, 8406–8413.

56 K. Fujimoto, Y. Ueda, D. Inohara, Y. Fujii and M. Nakayama, *Electrochim. Acta*, 2020, **354**, 136592.

57 M. Nakayama, K. Fujimoto, T. Kobayakawa and T. Okada, *Electrochem. Commun.*, 2017, **84**, 24–27.

58 A. Li, S. Kong, C. Guo, H. Ooka, K. Adachi, D. Hashizume, Q. Jiang, H. Hongxian, J. Xiao and R. Nakamura, *Nat. Catal.*, 2022, 109–118.

59 J. Murray and P. Brewer, in *Mar. Manganese Depos.*, ed. G. Glasby, Elsevier, Amsterdam, 1977.

60 R. G. Burns, *Geochim. Cosmochim. Acta*, 1976, **40**, 95–102.

61 R. G. Burns, *Nature*, 1965, 999.

62 J. Hanawalt, H. Rinn and L. Frevel, *Anal. Chem.*, 1938, **10**, 457.

63 H. Yin, W. Tan, L. Zheng, H. Cui, G. Qiu, F. Liu and X. Feng, *Geochim. Cosmochim. Acta*, 2012, **93**, 47–62.

64 H. Yin, H. Li, Y. Wang, M. Ginder-Vogel, G. Qiu, X. Feng, L. Zheng and F. Liu, *Chem. Geol.*, 2014, **381**, 10–20.

65 C. E. Frey, M. Wiechen and P. Kurz, *Dalton Trans.*, 2014, **43**, 4370–4379.

66 C. M. Julien, M. Massot and C. Poinsignon, *Spectrochim. Acta*, 2004, **60**, 689–700.

67 K. Nakamoto, *Infrared and Raman Spectra of Inorganic and Coordination Compounds Part A : Theory and Applications*, John Wiley & Sons, New Jersey, 6th edn, 2009.

68 C. E. Frey, F. Kwok, D. González-Flores, J. Ohms, K. Cooley, H. Dau, I. Zaharieva, T. Walter, H. Simchi, S. Mohney and P. Kurz, *Sustainable Energy Fuels*, 2017, **1**, 1162–1170.

69 T. Takashima, K. Hashimoto and R. Nakamura, *J. Am. Chem. Soc.*, 2012, **134**, 1519–1527.

70 A. Yamaguchi, R. Inuzuka, T. Takashima, T. Hayashi, K. Hashimoto and R. Nakamura, *Nat. Commun.*, 2014, **5**, 4256.

71 T. Takashima, K. Hashimoto and R. Nakamura, *J. Am. Chem. Soc.*, 2012, **134**, 18153–18156.

72 U. Maitra, B. S. Naidu, A. Govindaraj and C. N. R. Rao, *Proc. Natl. Acad. Sci. U. S. A.*, 2013, **110**, 11704–11707.

73 J. W. Murray and J. G. Dillard, *Geochim. Cosmochim. Acta*, 1979, **43**, 781–787.

74 C. L. Peacock and D. M. Sherman, *Chem. Geol.*, 2007, **238**, 94–106.

75 J. Cai, J. Liu, W. S. Willis and S. L. Suib, *Chem. Mater.*, 2001, **13**, 2413–2422.

76 N. Wiberg and A. F. Hollemann, *Lehrbuch der anorganischen Chemie*, Walter de Gruyter, 102nd edn, 2007.

77 S.-L. Kuo and N.-L. Wu, *J. Electrochem. Soc.*, 2006, **153**, A1317.

78 Y. Surendranath, M. W. Kanan and D. G. Nocera, *J. Am. Chem. Soc.*, 2010, **132**, 16501–16509.

79 M. Risch, K. Klingan, F. Ringleb, P. Chernev, I. Zaharieva, A. Fischer and H. Dau, *ChemSusChem*, 2012, **5**, 542–549.

80 M. Görlin, J. F. De Araujo, H. Schmies, D. Bernsmeier, S. Dresp, M. Gliech, Z. Jusys, P. Chernev, R. Kraehnert, H. Dau and P. Strasser, *J. Am. Chem. Soc.*, 2017, **139**, 2070–2082.

81 M. Görlin, P. Chernev, J. F. De Araújo, T. Reier, S. Dresp, B. Paul, R. Krähnert, H. Dau and P. Strasser, *J. Am. Chem. Soc.*, 2016, **138**, 5603–5614.

82 E. Gileadi, *Electrode Kinetics for Chemists, Chemical Engineers and Materials Scientists*, VCH Publishers, Inc., Weinheim, 1st edn, 1993.

83 R. L. Doyle, I. J. Godwin, M. P. Brandon and M. E. Lyons, *Phys. Chem. Chem. Phys.*, 2013, **15**, 13737–13783.

84 L. R. Faulkner and A. J. Bard, *Electrochemical Methods: Fundamentals and Applications*, John Wiley & Sons, 2nd edn, 2001.

85 M. Wiechen, I. Zaharieva, H. Dau and P. Kurz, *Chem. Sci.*, 2012, **3**, 2330.

86 H. Simchi, K. A. Cooley, J. Ohms, L. Huang, P. Kurz and S. E. Mohney, *Inorg. Chem.*, 2018, **57**, 785–792.

87 M. W. Kanan and D. G. Nocera, *Science*, 2008, **321**, 1072–1075.

88 Y. Surendranath, D. A. Lutterman, Y. Liu and D. G. Nocera, *J. Am. Chem. Soc.*, 2012, **134**, 6326–6336.

89 L. Trotochaud, S. L. Young, J. K. Ranney and S. W. Boettcher, *J. Am. Chem. Soc.*, 2014, **136**, 6744–6753.

90 K. Klingan, F. Ringleb, I. Zaharieva, J. Heidkamp, P. Chernev, D. Gonzalez-Flores, M. Risch, A. Fischer and H. Dau, *ChemSusChem*, 2014, **7**, 1301–1310.

91 M. Pourbaix, *Atlas of Electrochemical Equilibria in Aqueous Solutions*, Pergamon Press Ltd., 1st edn, 1966.

92 A. Ramírez, P. Hillebrand, D. Stellmach, M. M. May, P. Bogdanoff and S. Fiechter, *J. Phys. Chem. C*, 2014, **118**, 14073–14081.

93 D. Wang, J. Zhou, Y. Hu, J. Yang, N. Han, Y. Li and T.-k. Sham, *J. Phys. Chem. C*, 2015, **119**, 19573–19583.

94 D. González-Flores, K. Klingan, P. Chernev, S. Loos, M. Mohammadi, C. Pasquini, P. Kubella, I. Zaharieva, R. Smith and H. Dau, *Sustainable Energy Fuels*, 2018, **2**, 1986–1994.

95 M. K. Bates, Q. Jia, H. Doan, W. Liang and S. Mukerjee, *ACS Catal.*, 2016, **6**, 155–161.

96 M. Risch, F. Ringleb, M. Kohlhoff, P. Bogdanoff, P. Chernev, I. Zaharieva and H. Dau, *Energy Environ. Sci.*, 2015, **8**, 661–674.

97 A. Bergmann, E. Martinez-Moreno, D. Teschner, P. Chernev, M. Gliech, J. F. de Araújo, T. Reier, H. Dau and P. Strasser, *Nat. Commun.*, 2015, **6**, 8625.

98 M. A. Petit and V. Plichon, *J. Electroanal. Chem.*, 1998, **444**, 247–252.

99 M. Yagi, E. Tomita and T. Kuwabara, *J. Electroanal. Chem.*, 2005, **579**, 83–88.

100 X. Lu and C. Zhao, *Nat. Commun.*, 2015, **6**, 1–7.

101 Y. Surendranath, M. Dinca and D. G. Nocera, *J. Am. Chem. Soc.*, 2009, **8**, 2615–2620.

102 L. C. Seitz, C. F. Dickens, K. Nishio, Y. Hikita, J. Montoya, A. Doyle, C. Kirk, A. Vojvodic, H. Y. Hwang, J. K. Norskov and T. F. Jaramillo, *Science*, 2016, **353**, 197–203.

103 M. Huynh, C. Shi, S. J. L. Billinge and D. G. Nocera, *J. Am. Chem. Soc.*, 2015, **137**, 14887–14904.

104 L. Han, P. Tang, Á. Reyes-Carmona, B. Rodríguez-García, M. Torréns, J. R. Morante, J. Arbiol and J. R. Galan-Mascaros, *J. Am. Chem. Soc.*, 2016, **138**, 16037–16045.

105 M. Huynh, D. K. Bediako and D. G. Nocera, *J. Am. Chem. Soc.*, 2014, **136**, 6002–6010.

106 S. Cherevko, S. Geiger, O. Kasian, N. Kulyk, J.-P. Grote, A. Savan, B. Ratna, S. Merzlikin, B. Breitbach, A. Ludwig and K. J. J. Mayrhofer, *Catal. Today*, 2016, **262**, 170–180.

107 S. Cherevko, S. Geiger, O. Kasian, A. Mingers and K. J. Mayrhofer, *J. Electroanal. Chem.*, 2016, **773**, 69–78.

108 S. Cherevko, S. Geiger, O. Kasian, A. Mingers and K. J. Mayrhofer, *J. Electroanal. Chem.*, 2016, **774**, 102–110.

109 B. Zhang, Y. Li, M. Valvo, L. Fan, Q. Daniel, P. Zhang, L. Wang and L. Sun, *ChemSusChem*, 2017, **10**, 1–8.

110 M. W. Louie and A. T. Bell, *J. Am. Chem. Soc.*, 2013, **135**, 12329–12337.

111 F. Dionigi, T. Reier, Z. Pawolek, M. Gliech and P. Strasser, *ChemSusChem*, 2016, **9**, 962–972.

112 F. Urbain, V. Smirnov, J.-P. Becker, A. Lambertz, F. Yang, J. Ziegler, B. Kaiser, W. Jaegermann, U. Rau and F. Finger, *Energy Environ. Sci.*, 2016, **9**, 145–154.

113 B. Turan, J.-P. Becker, F. Urbain, F. Finger, U. Rau and S. Haas, *Nat. Commun.*, 2016, **7**, 12681.